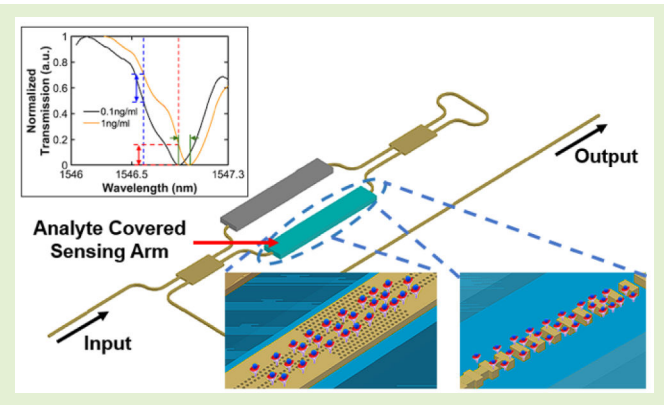


Experimental Comparison of Slow Light and Subwavelength Waveguide Interferometer Sensors

Jianhao Shen[®], Student Member, IEEE, Asela Perera[®], Arushi Rai, Madhuri Kango-Singh, and Swapnajit Chakravarty, Senior Member, IEEE

Abstract—We experimentally demonstrate slow light photonic crystal waveguide (PCW) and subwavelength waveguide (SWWG) loop terminated Mach-Zehnder interferometer (LT-MZI) sensors in a foundry-fabricated silicon-on-insulator (SOI) platform. We compare the experimental results on sensitivity and limit of detection (LOD) on the interferometer sensors with microcavity-type sensors. We show experimentally that 2-D PCW interferometers have higher phase sensitivities than SWWGs of the same length. Based on experimental results, 20-\(\mu\mathrm{m}\)-long 2-D PCW LT-MZI sensors and 200- μ m-long SWWG LT-MZI sensors achieve an LOD of 3.4 \times 10⁻⁴ and 2.3 \times 10⁻⁴ RIU, respectively, with nearly the same insertion losses in foundry-fabricated devices. We show that by considering the various sources of loss in our benchtop fiber-to-fiber photonic integrated circuit mea-



surement system, it will be possible to reach 10⁻⁷ LOD in both slow light PCW and SWWG-based LT-MZI sensors with on-chip integrated light sources and detectors. We show via simulations and experiment that the LOD of a 20-µm-long slow light PCW LT-MZI is equivalent to that of a 100- μ m-long SWWG LT-MZI, thus enabling more compact LT_MZI sensors when using slow light PCWs versus SWWGs.

Index Terms— Biosensors, chemical sensors, loop terminated Mach-Zehnder interferometer (LT-MZI), optical interferometer sensors, photonic crystal waveguide (PCW), silicon photonics, subwavelength waveguide (SWWG).

I. INTRODUCTION

URING the past two decades, with the progress of silicon photonics, various integrated photonic sensors have been experimentally demonstrated on the silicon-on-insulator (SOI) platform [1], [2], [3], [4], [5], [6], [7], [8]. The two types of devices primarily investigated are microcavity sensors and interferometer sensors. Microcavity devices include strip waveguide ring resonators (RRs) and racetrack resonators [1], [2], photonic crystal (PC) nanocavity resonators [3], [4], [5], and subwavelength waveguide (SWWG) cavity resonators [6], [7]. Interferometer devices have primarily been demonstrated

Manuscript received 2 August 2024; accepted 20 August 2024. Date of publication 2 September 2024; date of current version 16 October 2024. This work was supported by the National Science Foundation (NSF) under Grant 2210707 and Grant 2315085. The associate editor coordinating the review of this article and approving it for publication was Dr. Daniele Tosi. (Corresponding author: Swapnajit Chakravarty.)

Jianhao Shen, Asela Perera, and Swapnajit Chakravarty are with the Department of Electro-Optics and Photonics, University of Dayton, Dayton, OH 45469 USA (e-mail: shenj5@udayton.edu; pereraa2@ udayton.edu; schakravarty1@udayton.edu).

Arushi Rai and Madhuri Kango-Singh are with the Department of Biology, University of Dayton, Dayton, OH 45469 USA.

Digital Object Identifier 10.1109/JSEN.2024.3450186

using the Mach–Zehnder interferometer (MZI) configuration with strip waveguides and 1-D PC waveguides (PCWs) or the bimodal interferometry configuration [9], [10], [11], [12], [13], [14], [15].

In both interferometric and microcavity-type sensors, the interaction of the optical mode with the analyte results in changes in the effective refractive index of the optical mode as a result of changes in the analyte refractive index. In biosensors, the silicon waveguide surface, in both microcavity and interferometer configurations, is functionalized to attach receptor biomarkers that bind the specific conjugate probe biomarkers in the analyte solution. With the attachment of receptor and probe biomarkers to the silicon photonic waveguide surface, small changes in the biomarker adsorption results in small changes in the effective refractive index of the optical mode compared to the somewhat larger changes in the effective refractive index due to the bulk analyte changes in chemical sensing for instance. For biosensors, the limit of detection (LOD) is thus a critical performance metric that determines the minimum change in refractive index that can be detected by the platform, which translates correspondingly to picograms to micrograms per milliliter concentrations when detecting the binding between probe and target biomarkers. Microcavity sensors typically require high quality factor resonances that make them extremely sensitive to temperature fluctuations in addition to system noises. In contrast, temperature effects can be ignored with low quality factor interference fringes in interferometer sensors that are thus only influenced by system amplitude noise. Interferometer sensors have shown the potential to reach the lowest LOD of 10⁻⁷ RIU [9]; however, such low LODs require MZIs of several millimeters' length.

Two types of nanostructured devices have been recently used extensively for the demonstration of biosensors for diverse applications: 1) slow light PC devices where one relies on the enhanced interaction with the analyte due to the slow down of light [16] and 2) SWWG devices where one relies on the larger analyte-mode optical overlap integrals resulting from the larger analyte fill factors compared to evanescent wave devices [17]. Recently, we experimentally demonstrated loop-terminated MZI (LT-MZI) chemical sensors with slow light 2-D PCWs wherein we showed that slow light LT-MZI sensors demonstrated the highest phase sensitivity 277 750 rad/RIU-cm compared to all interferometer sensors in a compact platform [16].

In this article, we design and experimentally demonstrate LT-MZI biosensor devices in both the slow light and SWWG configurations and compare their relative performances and form factors. We show that the higher phase sensitivity of slow light PCW interferometers (277 750 rad/RIU-cm) compared to SWWG interferometers (72 600 rad/ RIU-cm), both in the LT-MZI configuration, results in higher sensitivities in more compact form factors for the PCW-based (20 μm length) LT-MZI than the SWWG LT-MZI, with nearly similar insertion losses in foundry-fabricated sensor devices.

Fig. 1(a) shows a schematic of the LT-MZI chem-bio analyte sensor [16]. Light from an input source is split into two equal paths via a 2×2 MMI 50:50 power splitter (labeled MMI_A) into a reference arm and a signal arm. The reference arm is covered with silicon dioxide so that it does not come in contact with any analyte and is thus not influenced by any changes in the ambient analyte. The nanostructures in the signal arm are not clad with oxide and thus come into direct contact with the analyte. The reference and signal arms are combined via a second 2×2 MMI power combiner (MMI_B). The output arms of MMI_B combine via a loop mirror that reflects the light back into the interferometer arms, in contrast to the MZI where the light is detected at the output, as shown in Fig. 1(b). Finally, the output is collected from MMI_A as shown in the schematic. In one configuration in Fig. 1(c), slow light PCWs are integrated on the reference arm and the signal arm, respectively. In the second configuration in Fig. 1(d), SWWGs are integrated on the reference arm and the signal arms. The reflected optical path in the LT-MZI doubles the optical path length versus the corresponding MZI with the same geometric path lengths and thus doubles the phase sensitivity in the LT-MZI. As noted in [16] and [18], the spectral resolution of the interferometer is given by the minimum resolvable change in intensity dI due to a shift in frequency $d\omega$ and is given by

$$\frac{dI}{d\omega} = \frac{I_0}{2} \frac{n_g L}{c} \sin \Delta \psi_s. \tag{1}$$

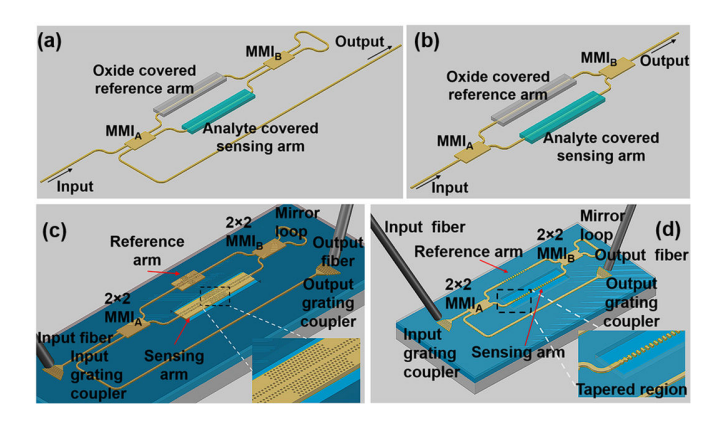


Fig. 1. Schematic layouts comparing (a) LT-MZI with (b) MZI. (c) and (d) Schematic drawings of studied 2-D PCW-based slow light and subwavelength waveguide-based LT-MZIs.

The spectral selectivity of the interferometer is thus proportional to the product $n_g L$, where n_g is the group index of the propagating optical mode in an interferometer with sensing arm length L and c is the velocity of light. $\Delta \psi_s$ represents the phase changes in the guided arm given by

$$\Delta \psi_S = \frac{2\pi}{\lambda} \Delta N_s(\omega) L \tag{2}$$

where λ is the wavelength of light and ΔN_s is the change in the effective index of the guided mode in contact with the analyte. In slow light high group index PCWs, a higher n_g enables a smaller L for more compact interferometer sensors than strip waveguide interferometers. In SWWGs, a higher fill factor of the analyte with the propagating optical mode enables a larger ΔN_s compared to strip waveguide interferometers.

II. DESIGN METHODOLOGY

A. Design of Enhanced Phase Shifted LT-MZI

The mathematical model of the LT-MZI can be intuitively described using transfer matrices [19]. Considering *a* and *b* as coupling coefficients, the transfer matrix of both MMI couplers can be expressed as

$$T_{\text{mmi}} = \begin{bmatrix} a & jb \\ jb & a \end{bmatrix}. \tag{3}$$

The coupling coefficients are dependent on multiple factors, including how much loss the MMI experiences and how exactly the power is split between the ports. For a lossless MMI coupler, $a^2 + b^2 = 1$, and if the coupler has accurate 3-dB splitting and a 90° phase shift between the outputs, $a = b = (1/\sqrt{2})$. Assuming both of these conditions and considering the naming convention of each of the MMI's in Fig. 1, (3) can be rewritten as

$$T_{\text{mmi}} = T_A = T_B = \frac{1}{\sqrt{2}} \begin{bmatrix} 1 & j \\ j & 1 \end{bmatrix}$$
 (4)

where T_A and T_B are represent transfer matrices of the first MMI (MMI_A) and second MMI (MMI_B), respectively. For the middle phase shifting section of the device [19], the transfer matrix T_{PS} is shown in the following:

$$T_{\rm PS} = \begin{bmatrix} e^{j\phi_1} & 0 \\ 0 & e^{j\phi_2} \end{bmatrix} = e^{j\phi_2} \begin{bmatrix} e^{j\Delta\phi} & 0 \\ 0 & 1 \end{bmatrix}. \tag{5}$$

Here, $\phi_1 = \beta_1(\lambda)L_1$ and $\phi_2 = \beta_2(\lambda)L_2$. $\Delta \phi = \phi_1 - \phi_2$ is the phase difference between the two interferometer arms. $\beta(\lambda)$

is the wavelength dispersion dependent propagation constant of the fundamental mode (the transverse electric (TE) mode in our device) determined by the silicon material. L_1 and L_2 are the lengths of the two interferometer arms. The power at ports B_1 and B_2 before the loop mirror to the input power at A_1 and A_2 can be shown as follows:

$$\begin{bmatrix} B_1 \\ B_2 \end{bmatrix} = T_B T_{PS} T_A \begin{bmatrix} A_1 \\ A_2 \end{bmatrix} = T_B T_{PS} T_A \begin{bmatrix} P^{\text{in}} \\ 0 \end{bmatrix}$$
$$= \frac{1}{2} e^{j\phi_2} \begin{bmatrix} e^{j\Delta\phi} - 1 \\ j(1 + e^{j\Delta\phi}) \end{bmatrix}. \tag{6}$$

On the forward path, as in an MZI, the outputs oscillate with a frequency determined by the phase difference $\Delta \phi$ between the interferometer arms. However, on the reflected (backward) path, the loop mirror switches the output matrix elements so that the transfer matrix relationship can be written as

$$\begin{bmatrix} A_1 \\ A_2 \end{bmatrix} = T_A T_{PS} T_B \begin{bmatrix} B_2 \\ B_1 \end{bmatrix} = \frac{1}{2} e^{j\phi_1} \begin{bmatrix} j\left(e^{2j\Delta\phi} - 1\right) \\ -\left(1 + e^{2j\Delta\phi}\right) \end{bmatrix}. \tag{7}$$

As observed from (7), the reflected light at MMI_A on both arms A_1 and A_2 oscillates at a frequency of $2\Delta\phi$. An optical circulator in our experiments connected to the input fiber prevents reflection back to the source. The lower output A_2 is monitored to determine the output of the LT-MZI.

From (7), the reflected powers P^{out} at the two arms of MMI_A are related to the input power P^{in} by the following:

$$P_{A_1}^{\text{out}} = \frac{1}{2} P^{\text{in}} [1 - \cos 2\Delta \phi]$$
 (8)

$$P_{A_1}^{\text{out}} = \frac{1}{2} P^{\text{in}} [1 - \cos 2\Delta \phi]$$

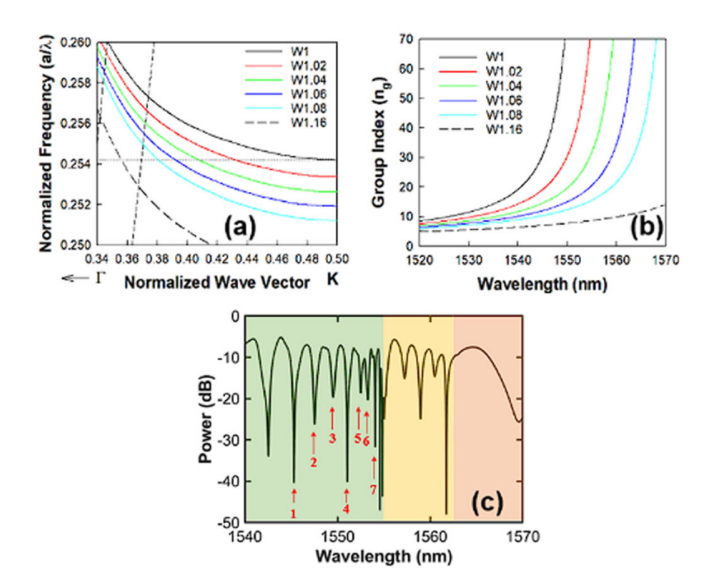
$$P_{A_2}^{\text{out}} = \frac{1}{2} P^{\text{in}} [1 + \cos 2\Delta \phi].$$
(8)

Equation (7) shows that since the light is reflected by the loop mirrors, it travels an effective path length that is twice that of an equivalent MZI with the same geometric length of the interferometer arms. As a result, the phase delay in the LT-MZI is doubled compared to the equivalent MZI resulting in twice the phase shift versus competing MZI structures. In silicon strip waveguide interferometers, the fringe separation is a function of wavelength due to material and waveguide dispersion. Similarly, in slow light and SWWG structures, the material dispersion and the waveguide dispersion of the respective geometries determine the phase change $\varphi = \beta L$ in each arm of the interferometer and the resultant interferometric fringe pattern.

B. PC Loop-Terminated MZI Design

The slow light 2-D PC waveguides defined in 220-nm silicon in SOI are 5 μ m long and 20 μ m long on the reference arm and signal arm, respectively. The lattice constant a of the PC air holes is 395 nm, and the air hole radius r = 0.275a.

Fig. 2(a) plots the dispersion diagram of the designed oxide clad and analyte clad W1 PCW arms simulated by Ansys Lumerical finite-difference time domain (FDTD). W1 indicates that the width of the PCW, given by the row of missing air holes as indicated in the schematic in Fig. 1, is $\sqrt{3}a$. Fig. 2(b) plots the group index versus wavelength of the analyte arm. The group index (n_g) is calculated from the normalized dispersion diagram in Fig. 2(a) as $n_g = (c/v_g) =$ $(c/(\partial \omega/\partial k))$, where $v_g = (\partial \omega/\partial k)$ denotes the group velocity, c is the velocity of light in free space, ω denotes the frequency,



(a) Normalized dispersion diagram of the water clad 2-D PCW in SOI. (b) Simulated group index versus wavelength for different adiabatically tapered W1 PCW width varying from $\sqrt{3}a$ to 1.08 \times $\sqrt{3}a$. Simulated transmission spectra of the 2-D PCW LT-MZI with a=390 nm, and arm lengths 5 and 15 μ m for the oxide clad reference arm and the water clad signal arm, respectively.

and k denotes the wavevector. Fig. 2(b) shows that the group index increases as one approaches the photonic band edge. To couple light efficiently into the high group index propagating wavelengths from the access strip waveguides, the PCW width is increased from W1 (= $\sqrt{3}a$) to W1.08 (=1.08 × $\sqrt{3}a$) over 16 lattice periods so that at the high group index wavelengths close to the photonic stopband edge, the group index can taper gradually to $n_g \sim 4$ of the strip waveguide [20], [21]. Fig. 2(b) shows representative group index profiles as the PCW width is increased from W1 to W1.08. Fig. 2(c) plots the FDTD simulated interference fringes of the LT-MZI that incorporates the group index dispersion computed in Fig. 2(b). The FDTD approach with integrated material dispersion accurately accounts for waveguide dispersion in the strip waveguide and slow light waveguide sections as also the waveguide bends in each interferometer arm in Fig. 1. In addition, FDTD accounts accurately for the loop mirror and the splitting ratios of the designed MMI_A and MMI_B. The green shaded and orange shaded regions in Fig. 2(c) denotes wavelength bandwidths over which light propagates in both the reference and signal arms, and in only the reference oxide clad arm. In the red-shaded region, the photonic stopband in both analyte- and oxide-filled arms restricts light propagation. The corresponding simulated transmission profiles for the oxide clad reference arm and the analyte water clad signal arms are shown to confirm the various shaded regions.

C. SWWG LT-MZI Design

The SWWGs are defined by a periodic layout of silicon pillars with period Λ and fill factor f. SWWG propagation is achieved when the lattice period $\Lambda < (\lambda/2n_{\rm eff})$ ($n_{\rm eff} =$ effective refractive index in the silicon waveguide) and the propagating light see the SWWG as a conventional waveguide at the propagating wavelength. Fig. 3(a) shows the dispersion diagram of an SWWG with different lattice constants.

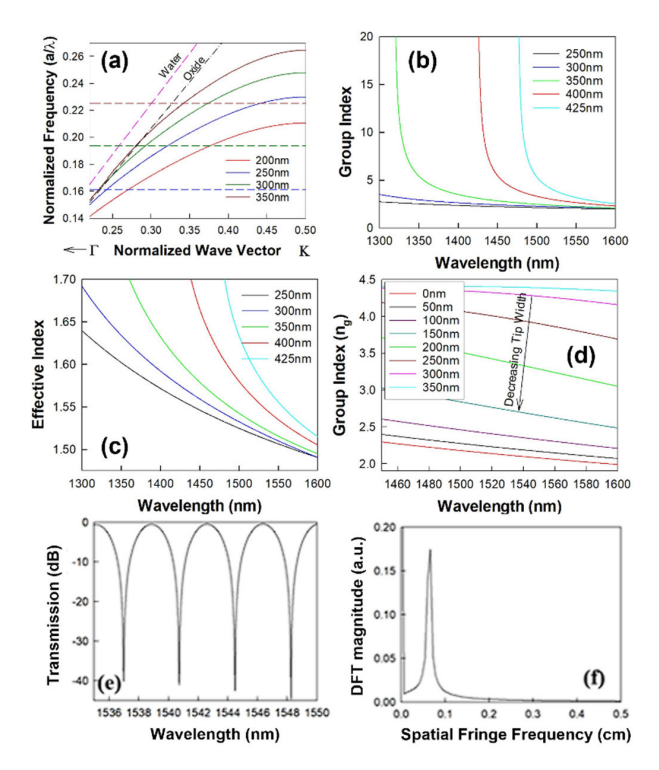


Fig. 3. (a) Normalized dispersion diagram for the SWWGs at different lattice constants with the $\lambda\sim1540\text{-nm}$ operating point indicated by a dashed line for corresponding colored dispersion plots. (b) Group index and (c) effective index versus wavelength of the periodic 1-D nanostructures for different lattice constants. (c) Group index versus wavelength for different adiabatically tapered tip widths for the SWWG with $\lambda=300$ nm. (d) Simulated transmission spectra of the SWWG LT-MZI with $\lambda=300$ nm, and arm lengths 50 and 200 μm for the oxide clad reference arm and the water clad signal arms, respectively. (f) DFT of the transmission spectrum in (e).

At our operating wavelengths $\lambda = 1550$ nm, lattice periods $\Lambda < 318$ nm enable light propagation in the subwavelength regime. Fig. 3(b) and (c) plots the group index and effective index versus wavelength for different lattice constants showing that typical group indices in water clad silicon SWGs is $n_{\rm g} \sim 2.1$, respectively. As a result, similar to 2-D PCWs in Section II-A, the group index must be engineered to enable efficient coupling from the strip waveguide to the SWWG and reduce reflection losses at the strip waveguide and SWWG interface. The strip waveguide is tapered from a width of 500 nm to a narrow tip width in the SWWG region. As observed in Fig. 3(c), the group index decreases to 2.1 when the taper tip width decreases to zero. Based on minimum feature sizes achievable reliably in fabrication \sim 150 nm, a taper tip width of 150 nm was designed, which resulted in a group index difference $\Delta n_g \sim 0.5$ at the operating wavelength. Fig. 3(d) shows simulated interference fringes in the designed LT-MZI SWWG. Fig. 3(f) shows the discrete Fourier transform (DFT) of the simulated fringe spectrum showing a single broad spatial period corresponding to a fringe period that varies between 15.5 and 15.75 cm⁻¹ within the simulated domain. As expected, no other spatial frequencies are observed in the Fourier transform in Fig. 3(f).

III. EXPERIMENTAL RESULTS

A. Biosensing Procedure

The procedure starts with an appropriate cleaning and surface activation of the silicon surface for the silane growth.

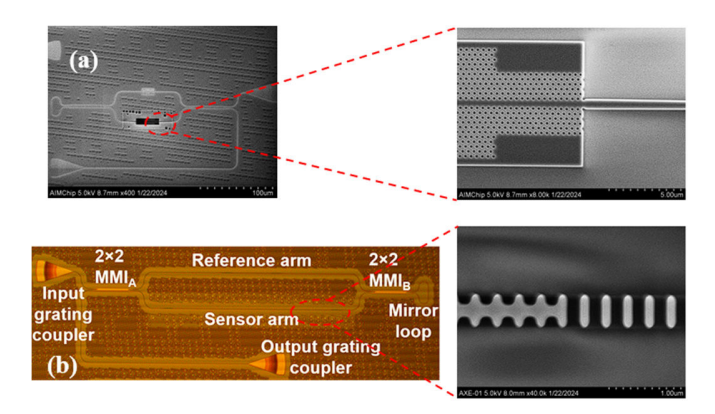


Fig. 4. (a) and (b) SEM images for the 2-D PCW LT-MZI and the SWWG LT-MZIs, respectively. Zoomed-in SEMs of marked regions in (a) and (b) show both the sensing arms and also the adiabatic tapered coupling region in both structures to enhance coupling efficiency into both devices from access strip waveguides.

The chip was rinsed thoroughly with acetone, methanol, and isopropyl alcohol (IPA) in sequence. Then, the chip was dried under a stream of nitrogen gas, followed by oxygen plasma ashing treatment for 10-min duration at 80-sccm, 300-mT, and 270-mW RF to reduce the surface roughness and control the activation of the -OH group on the silicon surface. After the formation of -OH, 10% solution of (3-aminopropyl) triethoxysilane, which is known as APTES diluted in pure toluene, is dispensed to the surface of the chip for 1 h at room temperature to convert the -OH to -NH2 on the surface. A thorough rinse with methanol and toluene in sequence is done and then followed by nitrogen gas blow till dry. The chip is then baked at 110 °C for 1 h; 2.5% (v/v) of glutaraldehyde in phosphate-buffered saline (PBS) is dispensed on the chip for 30 min at room temperature. This is then followed by rinsing the chip with DI water and blowing with nitrogen gas. The -NH₂ bonds on the surface are then substituted with -CHO bonds after the reaction with glutaraldehyde. The primary antibody biotin N-hydroxysuccinimide ester from Sigma-Aldrich diluted in PBS as a concentration of 0.1 mg/mL is coated on the chip in a 4 °C fridge for 1 h. The chip is washed with PBS three times and blew with nitrogen. A 2-mg/mL bovine serum albumin (BSA) in PBS is coated on the chip in 4 °C fridge for 1 h to prevent the nonspecific binding. The standard streptavidin powder from streptomyces avidinii (Sigma-Aldrich) was prepared into 0.1, 1, 2.5, 5, 7.5, and 10 ng/mL in a solution of PBS with 1% (v/v) BSA in PBS as the solvent. The spectrum was collected each time after the streptavidin was coated on the chip at 4 °C in the fridge for 1.5 h to guarantee sufficient conjugate binding with the Biotin. Fig. 4(a) shows the SEM image of the 2-D PCW LT-MZI device and the zoomed-in PCW region. Fig. 4(b) shows the microscope image of the SWWG LT-MZI device and the SEM image of the zoomed-in SWWG region.

B. PC Loop-Terminated MZI Biosensing

Fig. 5(a) shows a typical experimental interference fringe spectrum observed in our slow light 2-D LT-MZI biosensor. Fig. 5(a) also shows an experimentally measured transmission spectrum of two straight 15- μ m-long PCW devices identical to the reference arm being clad with silicon dioxide and identical

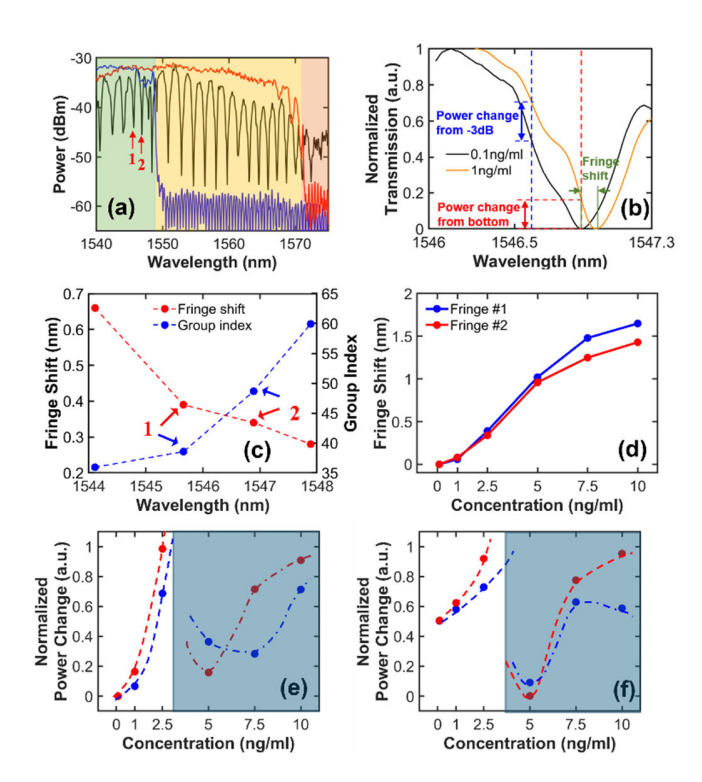
to the signal arm being clad with PBS. By comparing with simulations in Fig. 2(c), we are clearly able to identify the three regions of propagation in the 2-D PCW LT-MZI biosensor as demarcated in green, yellow, and orange in Fig. 5(a). The bulk sensitivity of the interference fringes was previously obtained as \sim 100 nm/RIU on average [14]. Fig. 5(b) shows the linearized and normalized fringe 2 labeled in Fig. 5(a) at the concentration of 0.1 and 1 ng/mL of the biomarker. The fringe shift, power change from -3 dB, and power change from the bottom point are shown in Fig. 5(b). Apparently, the power change from -3-dB point is larger than that from the bottom point with increasing concentration. Fig. 5(c) plots the change in absolute wavelength shift as a function of the fringes that are numbered as increasing integers approaching the photonic stopband edge. The two fringes labeled in Fig. 5(a) are marked in Fig. 5(c). The group index is calculated from the wavelength spacing $\Delta \lambda$ in the interference fringes as

$$n_g = \frac{\lambda^2}{2\Delta\lambda L}.\tag{10}$$

From Fig. 5(c), we observe that the group index increases with increasing fringe number as one approaches the photonic stopband edge. From the experimentally observed data in Fig. 5(d), we observe that for increasing concentration of streptavidin, the absolute wavelength shift observed for the fringes decreased with decreasing wavelength offset from the photonic stopband edge of the signal arm. As biomarker concentration is gradually increased, the fringes closest to the band edge with the highest phase sensitivity are redshifted across the photonic stopband edge at concentrations >10 ng/mL. These fringes would therefore be most suitable for interrogating low biomarker concentrations. The interference fringes designated as 1 and 2 in Fig. 5(a) were next monitored for changes in intensity at a fixed wavelength, as illustrated in Fig. 5(e) and (f). As observed, the monitored power at a fixed wavelength increases with increasing concentration but drops at higher concentrations when the shift exceeds the free spectral range (FSR) and fringes lower in wavelength start to overlap. If the PCW sensing arm length was shorter, then the FSR would be wider and the intensity at the higher concentrations would have reached the unity normalized value. The corresponding concentration therefore marks the upper limit of the dynamic range of our demonstrated biosensor. The plots in Fig. 5(e) considered the change in intensity as measured starting from the initial concentration value at the fringe minimum wavelength where the intensity is a minimum. In Fig. 5(f), the change in intensity for fringes 1 and 2 is plotted starting from the -3-dB operating point of each fringe, as explained in Fig. 5(b). In Fig. 5(e) and (f), we observe that the increase in monitored power for increasing concentrations is more for the fringe closer to the stopband edge where the group index is higher than the fringes farther away from the band edge.

C. SWWG LT-MZI Biosensing

Fig. 6(a) shows a typical interference fringe spectrum measured in our SWWG LT-MZI biosensor. While the fringe density in Fig. 6(a) is the same as observed from simulations in Fig. 3(e), additional fringes with a higher spatial frequency are superimposed on the primary LT-MZI fringes. Fig. 6(b) shows the measured fringe spectrum from Fig. 6(a) in a linear



(a) Experimental normalized fringe spectrum of the 2-D PCW LT-MZI at a concentration of 0.1 ng/mL in PBS. The normalized transmission characteristics of the oxide clad reference arm and the PBS clad signal arm are also shown to indicate the respective propagation regions. (b) Plot of the experimentally observed fringe 2 for concentrations of 0.1 and 1 ng/mL. The wavelength shift $(\Delta \lambda)$ is measured as shown in green. Dashed red and blue lines indicate the wavelengths at which intensity changes are monitored at the resonance wavelength and the -3-dB wavelength, respectively. (c) Change of group index and fringe wavelength for fringes numbered in increasing number approaching the stopband edge from 0.1 to 2.5 ng/mL. (d) Wavelength shift of the interference fringes, fringe 1 (blue) and fringe 2 (red) as a function of increasing concentration of streptavidin. (e) Change in intensity at fringe minimum wavelength for fringes 1 (blue) and 2 (red) as labeled in (a) with increasing concentrations of streptavidin. (f) Change in intensity at the -3-dB wavelength for fringes 1 (blue) and 2 (red) as labeled in (a) with increasing concentrations of streptavidin. The blue shaded region in (e) and (f) indicates the concentrations at which the previous fringe overlaps with the selected fringe due to limited FSR.

scale. Unlike the DFT spectrum of the simulated SWWG LT-MZI interferometer observed in Fig. 3(f), the DFT of the fringe spectrum in Fig. 6(b) shows several additional higher frequencies, which we believe arises from Fabry-Perot oscillations between the input and output fibers and also from reflections between the fibers and the SWWG and taper regions. The higher order spatial frequencies challenge the measurement of fringe shifts and/or fringe intensity changes versus different concentrations of biomarkers. By setting the higher order spatial frequencies to zero in the Fourier spectra in Fig. 6(d), we can retrieve the true LT-MZI fringe spectrum in Fig. 6(e) from an inverse DFT. Fig. 6(f) shows the corrected spectrum from Fig. 6(e) in log scale with the original spectrum from Fig. 6(a) superimposed. Fig. 6(f) shows that if one does not remove the higher frequencies, measurements may misconstrue the true wavelength shifts and also the true intensity changes and thus affect the understanding of measurement repeatability.

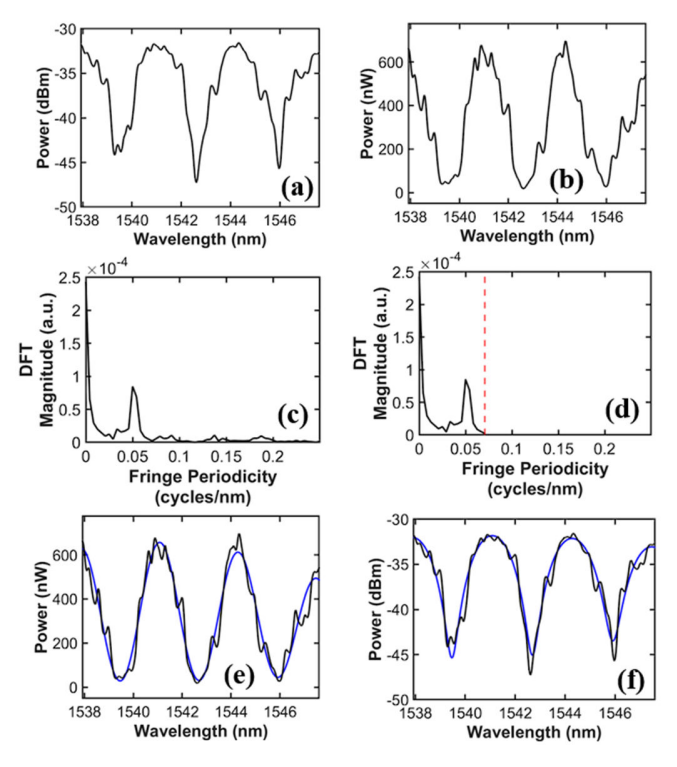


Fig. 6. (a) Experimental measured fringe spectrum of the SWWG LT-MZI in biosensing in log scale and (b) in linear scale. DFT of (c) measured spectrum in (a) and (b) showing the higher fringe periodicity frequencies and (d) with the higher fringe periodicity frequencies corrected/postprocessed to zero. The inverse DFT of the corrected fringe periodicity frequency spectra in (d) is shown in (e) linear scale and (f) log scale. (e) and (f) Super-impose the original measured spectra from (b) and (a), respectively.

Fig. 7(a) and (b) shows the measured and corrected interference fringes, respectively, in acetone and ethanol. From the shift in the interference fringes for acetone and ethanol, the bulk sensitivity is computed as 775 nm/RIU. Fig. 7(c) plots the simulated and experimentally measured bulk sensitivity for different periodicities of the SWWG LT-MZI. While the bulk sensitivity increases with increasing periodicity, the group index gradually increases as seen from simulations in Fig. 3(b) and one is no longer in the subwavelength regime as denoted by the red dashed line in Fig. 7(c). Fig. 7(d) shows the shift of interference fringes with streptavidin concentrations of 0.1, 10, and 100 ng/mL. The DFT corrected plots and the corresponding fringe shifts are plotted in Fig. 7(e). Fig. 7(f) shows the shift in the wavelength interference fringes as a function of increasing concentration of streptavidin. Changes in intensity at a fixed wavelength are depicted from Fig. 7(g) and (h) considering fringe minimum and 3-dB intensity point of the fringe, respectively. Similar to the 2-D PCW LT-MZI, the monitored power at a fixed wavelength increases with increasing concentration but drops at higher concentrations when the fringe shift exceeds the FSR, and the previous fringe starts to overlap. Similar to the 2-D PCW LT-MZI, if the sensing arm length was shorter, then the FSR would be wider and the intensity at the higher concentrations would have reached the unity normalized value as illustrated by the red dots in Fig. 7(g). However, increasing the FSR potentially compromises the LOD of the SWWG LT-MZI as we will see in Section IV-A. By comparing the lowest two concentrations in

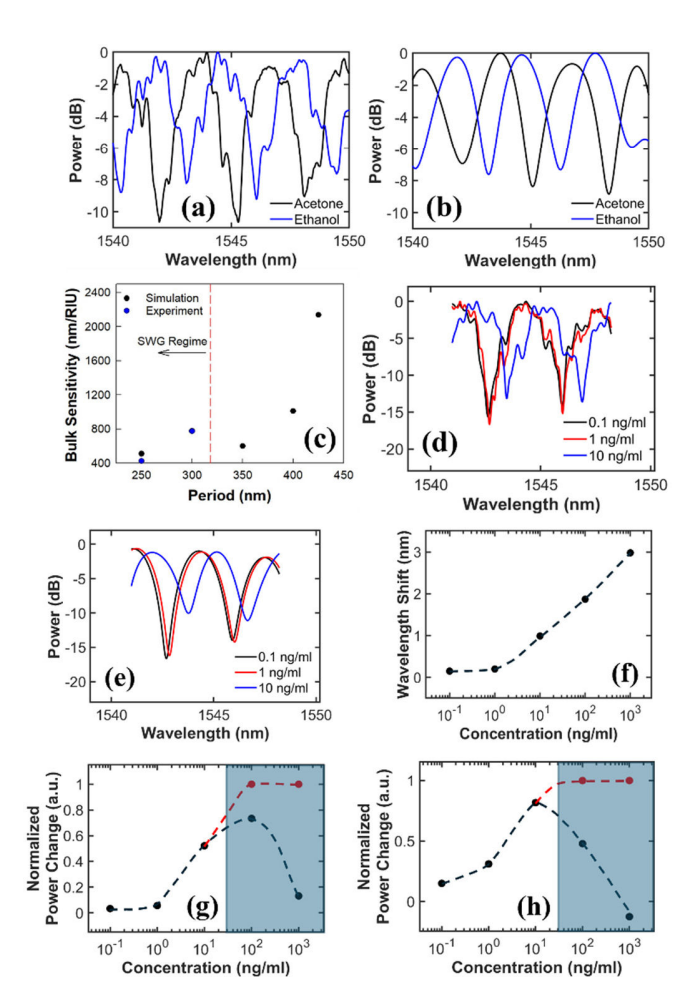


Fig. 7. (a) Experimental fringe spectrum of the SWWG LT-MZI in acetone and ethanol and (b) corresponding DFT corrected spectra. (c) Simulated and experimental bulk sensitivities for different SWWG LT-MZIs. (d) Normalized trans-mission spectra of the interference fringes for different concentrations of streptavidin and (e) corresponding DFT corrected fringe spectra. (f) Wavelength shift of interference fringes as a function of increasing concentrations of streptavidin. (g) Normalized change in intensity of the interference fringe at a fixed wavelength for increasing concentration of streptavidin when measured starting from the fringe minimum and (h) when measured from the 3-dB intensity point of the fringe. The blue shaded region in (g) and (h) indicates concentrations at which the previous fringe overlaps with the selected fringe due to limited FSR. Red dots in (g) and (h) indicate that the measured intensity would remain saturated if not overlapped with another fringe.

Fig. 7(g) and (h), we also observe that monitoring the intensity change at a fixed wavelength results in a more appreciable change in intensity when measured at the -3-dB operating point versus at the fringe minima.

We note that the DFT corrections applied here for the SWWG LT-MZI can also be applied for the 2-D PCW LT-MZI. The monotonically increasing group index (n_g) near the band edge however leads to a large change in group index [Fig. 2(b)] and hence FSR for the 2-D PCW LT-MZI. In contrast, n_g of the SWWG LT-MZI is practically constant in the $\lambda=1550$ nm range as indicated by the nearly flat n_g plots for $\Lambda=300$ nm in Fig. 3(b). A wider range of fringe periodicities would need to be corrected in the DFT of the 2-D PCW LT-MZI. However, this issue can be overcome by selecting the fringe of interest and DFT correcting for only the identified fringe in Fig. 3(a) for instance. The 2-D PCW LT-MZI fringes were not DFT corrected.

IV. DISCUSSION

A. Limit of Detection

In interferometric biosensing with slow light 2-D PCW sensors, the interference fringes are monitored as a function of varying concentration of probe biomarkers introduced in solution. Two parameters can be monitored: 1) the shift in wavelength of interference fringes as a function of change in biomarker concentration and 2) change in intensity of a fringe at a fixed wavelength. The former method requires either a tunable laser and photodetector or a broadband source and optical spectrum analyzer (OSA). Tunable lasers and OSAs are both expensive and bulky and preclude the feasibility of an eventual implementation as an at-home portable sensor. Benchtop OSAs are bulky and expensive as well. Arrayed waveguide grating (AWG) spectrometers [22] and Fourier transform infrared (FTIR) spectrometers [23] on a chip also require a significantly large area on the chip when monitoring sub-10-pm wavelength shifts required in high-sensitivity biosensing applications. While diverse sensor platforms have been employed to miniaturize small at-home portable devices [1], [2], [3], [4], [5], [6], [7], [8], [9], [10], [11], [12], [13], [14], [15], [16], [17], [18], [22], [23], [24], [25], [26], [27], [28], [29], in our present research, we investigated the LOD practically achievable in our PCW and SWWG LT-MZI devices.

As described in [16], the phase sensitivity of interferometric fringes can be written as

Phase Sensitivity

$$= \frac{\text{Bulk Sensitivity}}{\text{Free Spectral Range}} \times \frac{2\pi}{\text{Sensing Arm Length}}.$$
 (11)

The minimum phase shift that can be detected is determined by the minimum wavelength shift that can be detected and is given by

Minimum Phase Shift

$$= \frac{\text{Minimum Detectable Wavelength Shift}}{\text{Free Spectral Range}} \times 2\pi. \quad (12)$$

The LOD is given by

Limit of Detection

$$= \frac{\text{Minimum Phase Shift}}{\text{Phase Sensitivity} \times \text{Sensing Arm Length}}.$$
 (13)

The minimum detectable wavelength shift is thus limited by instrument resolution of the OSA. Typical state-ofthe-art OSAs have a wavelength resolution of 20 pm. From the experimentally demonstrated phase sensitivity of 277 750 rad/RIU-cm from the fringe shifts between acetone and IPA in [16], the LOD for 2-D PCW LT-MZIs computed from the wavelength shift is 2.4×10^{-4} RIU. The fringe shift measurements between ethanol and IPA was done at least three times to determine the LOD. If the minimum detectable wavelength shift is 1 pm, as measured by higher end OSAs, then the computed LOD from experimental data is 1.2×10^{-5} RIU. Similarly, for the SWWG LT-MZIs, the phase sensitivity was determined experimentally from three repeated measurements as 72 600 rad/ RIU-cm from which the LODs for minimum detectable wavelength shifts 20 and 1 pm are computed as 2.6×10^{-5} and 1.3×10^{-6} RIU, respectively.

In high quality factor (Q-factor) RR devices, where Q is in excess of 25000, sample absorption induced noise and

temperature drift induced noise affect the LOD. However, measured interference fringes in 2-D PCW LT-MZI devices have small linewidths with Q < 2000. In SWWG LT-MZI devices, the fringes have Q < 1000. Consequently, the above sources of noise can be neglected, and we can assume that the devices are primarily limited by the amplitude noise arising from factors such as the laser intensity noise, detector noise such as shot noise and thermal noise, and also from signal processing.

In our measurement setup with fiber adaptors and circulators in the optical fiber paths leading into and out of the pho-tonic chip, the source to detector insertion loss, including ~3-dB input and output grating coupler losses, is approximately 23 dB as shown in Fig. 8(a) (considering uniform input power 1 mW across all wavelengths of the tunable laser). Since devices are fabricated in a commercial CMOS foundry, insertion losses of the process development kit (PDK) incorporated grating couplers are nearly constant across all devices on a chip. As a result, any additional losses in measured devices can be attributed to intermediate devices and circuits between input and output grating couplers. Fig. 8(b) and (c) shows, respectively, the experimentally measured source to detector transmission through a 15- μ m-long straight 2-D PCW with a = 395 nm and through a 200- μ m-long straight SWWG with a fill factor f = 0.4 as used in our LT-MZI sensing with the cladded streptavidin at the concentration of 0.1 ng/mL. Fig. 8(d) and (e) shows the raw trans-mission spectra observed in the CMOS foundry-fabricated 2-D PCW and SWWG LT-MZI devices with 20- and 200- μ m-long signal arms, respectively, implying ~ 10 -dB insertion loss in both types of nanostructured devices for an input power 1 mW. Fig. 8(f) shows the transmitted power at a fixed wavelength versus time, at a similar power level as during our measurements, showing a variation <3 dBm during the measurement of light coupled through a straight waveguide with input and output grating couplers. The measured power fluctuations compute to \sim 136 nW noise level in absolute units, in our setup.

Fig. 9(a) and (b) shows the raw transmission of the demarcated fringes in Fig. 8(d) and (e), respectively, for the 2-D PCW LT-MZI and the SWWG LT-MZI. The linearized plots are shown in Fig. 9(c) and (d) for 2-D PCW LT-MZI and SWWG LT-MZI, respectively. The fringes when shifted in wavelengths corresponding to the power fluctuation in Fig. 8(f) arising from a hypothetical effective refractive index change are plotted as the dashed curves. From Fig. 8(d) for the 2-D PCW LT-MZI, we note that the monitored power at the fixed wavelength around the half-intensity operating point changes from -34.99 to -33.44 dBm (corresponding to 136-nW system noise fluctuation) for an 80-pm wavelength shift for the fringe closest to the band edge, labeled as fringe 2. The computed LOD is 3.4×10^{-4} RIU. For fringe 1, the corresponding required wavelength shift would be 100 pm, as expected from the reduced phase sensitivity leading to a lower LOD. For the SWWG LT-MZI, Fabry-Perot effects between fiber and fiber are superimposed on the LT-MZI interference spectra. The monitored power at a fixed wavelength around the half-intensity operating point changes from -35 to -33.55 dBm for a 180-pm wavelength shift. The computed LOD is 2.3×10^{-4} RIU, nearly the same order as the 2-D PCW but on an order of magnitude longer length.

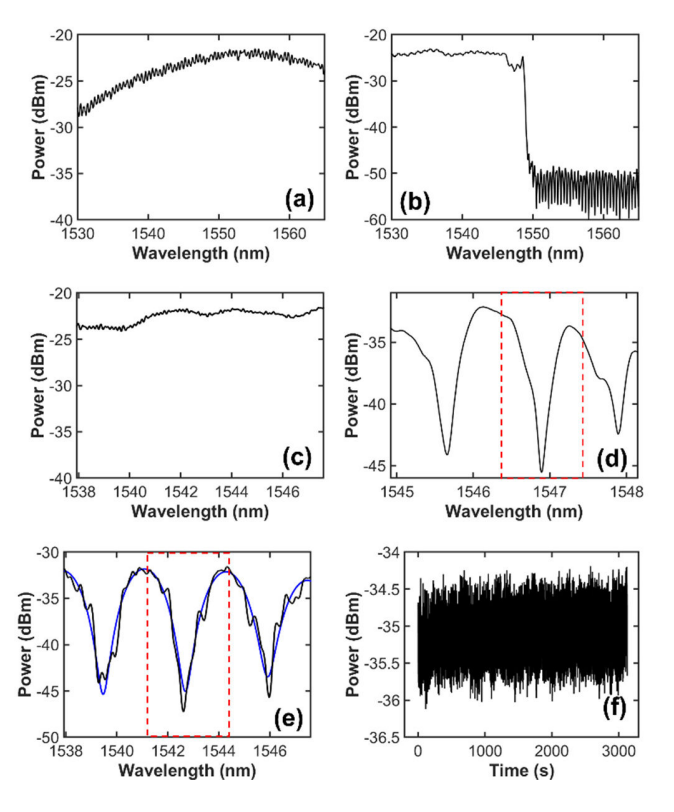


Fig. 8. Raw experimentally measured spectra showing (a) grating coupler transmission envelope, (b) transmission through a straight 0.1-ng/mL PBS clad 2-D PCW with PDK grating couplers, (c) transmission through a straight 0.1-ng/mL PBS clad SWWG, (d) transmission through the 2-D PCW LT-MZI with $20-\mu m$ sensing arm length, and (e) transmission through SWWG LT-MZI with $200-\mu m$ sensing arm length. The DFT corrected fringe is superimposed. The selected interference fringes for LOD analysis are emphasized with red dashed boxes in (d) and (e). (f) Measured system noise at the 3-dB operating point of the 2-D PCW LT-MZI fringe versus time.

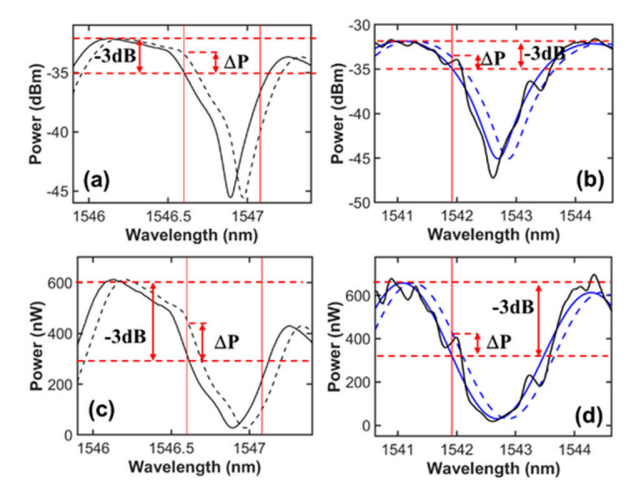


Fig. 9. Measured interference fringes (in black solid) for (a) 2-D PCW LT-MZI and (b) SWWG LT-MZI with the sensor arm clad with 0.1-ng/mL PBS. (c) and (d) Linearized plots of (a) and (b) for 2-D PCW LT-MZI and SWWG LT-MZI, respectively. The SWWG LT-MZI fringes were DFT corrected to overcome the fiber-to-fiber Fabry-Perot fringe effects and plotted in blue solid curves in (b) and (d). The hypothetical fringe shifts are indicated by black dashed and blue plots. The -3-dB operating points for LOD calculation are indicated by red solid lines.

We note that the measurements were done here in the -32- to -38-dBm range with a 23-dB system insertion loss

(including grating 3 dB at each coupler as known from the PDK). The fringe extinction (\sim 15 dB in the 2-D PCW LT-MZI and ~17 dB in the SWWG LT-MZI) does not change with an increase or decrease in the source power. Thus, if the 23-dB insertion loss can be eliminated, the signal-to-noise ratio (SNR) would improve and lower LOD values would be achieved. Chip-integrated lasers emitting in excess of 10 mW are already available [30] in silicon photonics. Onchip lasers have demonstrated 0.5-dB insertion loss to silicon waveguides [31]. The raw transmission curves that we have observed in our experiments will be shifted up in power to ~ 0.5 dBm and all LOD computations would hold with an additional two orders of magnitude enhancement in the LOD. For photodetectors, on-chip detectors have been demonstrated with a responsivity of 0.7 A/W and a dark current \sim 10 nA, which translates to about 15-nW detector noise limit [32], [33], approximately an order of magnitude lower than our benchtop measurement system. System noise can be reduced in several ways such as by reducing detector bandwidth, using balanced detection or band shifting with lock-in amplification [34]. Reduction in electrical and mechanical noise and coherent phase readout mechanisms enable optimization of the LOD [35], [36]. Hence, for both the SWG LT-MZI and the 2-D PCW LT-MZI, an order of magnitude enhancement in the LOD can be achieved from our measured values in our experimental setup. The integration of the on-chip laser and the on-chip photodetector would enable approximately three orders of magnitude enhancement in the experimentally measured LOD to reach the theoretical 10⁻⁷ RIU limits for both the SWWG LT-MZI and the 2-D PCW LT-MZI. The LOD is achieved without requiring spectrometers with picometer resolution or tunable lasers and represents a significant advantage compared to other measurement methods.

Our LT-MZI simulation models are generated from multimodule simulations using Ansys MODE, FDTD, and Interconnect. The amplitude noise limited LOD is calculated from transmission spectra at the -3-dB operating point of the interference fringe for the PCW LT-MZI with $20-\mu m$ sensing arm length (designated as PCW20Sim) and for the SWWG LT-MZI for various lengths 20, 100, and 200 μ m for the sensing arm (designated as SWWG20, SWWG100, and SWWG200, respectively) and plotted in Fig. 9. In our simulated model, we assume that 1 mW of power is coupled into the input waveguides with an insertion loss of 0.5 dB [31], and other insertion losses are ignored as described earlier. We also assume that the integrated photodetector noise is 15 nW [32], [33]. Simulated LODs for the 2-D PCW LT-MZI and SWWG LT-MZI are thus estimated as 2×10^{-7} RIU and 1.5×10^{-7} RIU, respectively. Fig. 10(a) shows that the phase sensitivity of SWWG LT-MZIs remains practically constant due to decreasing FSR with increasing length of the sensing arm. PCW LT-MZI simulations for our designed 2-D PCW LT-MZI indicate that while a higher phase sensitivity can be achieved compared to SWG LT-MZIs, the LOD of a 2-D PCW LT-MZI with a 20- μ m-long sensing arm is nearly equal to that of an SWWG LT-MZI with a 100- μ m-long sensing arm, as indicated in Fig. 10(b). To achieve better LOD in more compact form factors in the SWWG LT-MZI, the analyte fill fraction must be further increased from 60% (f = 0.4 in silicon) as in our demonstrated SWWG LT-MZI. Fill factors can be enhanced in the 2-D PCW LT-MZI by increasing the 79.5 nm/RIU (expt)

 Δn_{max}

0.0236 RIU

0.0028 RIU

0.0041 RIU

(expt)

TABLE I

COMPARISON OF PC SENSOR PLATFORMS

TABLE II
COMPARISON OF SWWG SENSOR PLATFORMS

1.75 nm at 1µg/ml (expt)

Device	Bulk sensitivity	Bio sensing (Δλ)	LOD	Δn_{max}
Genalyte Strip RR [1]	163nm/ RIU	0.12nm at 20mM	7.6 ×10 ⁻⁷ RIU	0.0005 RIU
Vernier RR [38]	2169nm/ RIU	_	8.3×10 ⁻⁶ RIU	0.001 RIU
SWWG RR [7]	405 nm/ RIU	1.4 nm at 20µg/ml	iLOD=2.5×10 ⁻⁴ RIU	0.0017 RIU
			sLOD=2.5×10 ⁻⁶ RIU	
SWWG race-track RR [6]	430 nm/ RIU	_	3.7×10 ⁻⁴ RIU	0.0061 RIU
SWWG LT-MZI, 200μm	775 nm/ RIU (expt)	$3 \text{ nm} - 1 \mu \text{g/ml (expt)}$	2.3×10 ⁻⁴ RIU (expt)	0.0019 RIU
long (this work)			1.5×10 ⁻⁷ RIU (sim)	(expt)

diameter of the holes. However, such an increased analyte fill factor will necessitate SWWG fins to be significantly narrower than 120 nm or gaps narrower than 120 nm between PC holes, which requires advanced foundry photonic device fabrication capability than the line-space fabrication dimension limitations stipulated to manufacture the present devices.

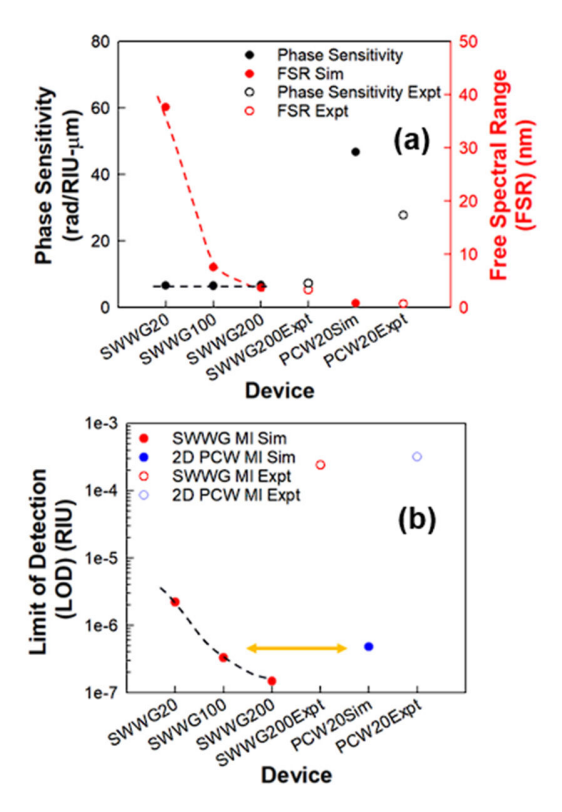
B. Comparison With Other Dielectric Sensors

PCW LT-MZI, 20µm long

(this work)

Our experimental results in foundry-fabricated devices established that in terms of absolute transmitted signal intensity, we observe no difference in SNRs in 2-D PCW devices and SWWG devices. In Tables I and II, we compare the performance of representative microcavity and interferometer devices on the PC and SWWG platforms. We observe that, in general, interferometer sensors achieve lower detection limits than microcavity sensors while being less susceptible to temperature noise drifts in high-Q microcavity sensors.

For low-cost fixed wavelength intensity measurement in an automated system, the upper LOD in interferometric sensors with low-Q fringes is roughly half the FSR after which the intensity retraces its values. In our slow light LT-MZI, from FSR = 0.65 nm and bulk sensitivity 79.5 nm/RIU, the maximum $\Delta n \; (\Delta n_{\rm max})$ that can be measured is $0.5 \times FSR/S_{bulk} = 4.1 \times 10^{-3}$ RIU. In the SWWG LT-MZI, from FSR = 3 nm and bulk sensitivity 775 nm/RIU, $\Delta n_{\rm max}$ is 1.92 \times 10⁻³ RIU. In high-Q resonator systems, for fixed wavelength intensity measurements, the peak power saturates at a certain Δn once the wavelength shift exceeds the resonance linewidth. Δn_{max} occurs for $\Delta \lambda$ that equals the difference in wavelength between the resonance minimum and maximum. For the comparative geometries listed in Tables I and II, the resonance line shapes in [1], [6], [7], [26], [36], and [37] were digitized and Δn_{max} determined from the published bulk sensitivities. Microcavity sensors typically measure the resonance wavelength shift with high cost tunable lasers for sensing; thus, Δn_{max} is higher with the upper limit



 $3.4 \times 10^{-4} \text{ RIU (expt)}$

2×10⁻⁷ RIU (sim)

Fig. 10. (a) Simulated and experimental phase sensitivity (left axis) and FSR (right axis) and (b) LOD in RIU for SWWG LT-MZIs of different lengths 20, 100, and 200 $\mu \rm m$ for the sensing arm (designated as SWWG20, SWWG100, and SWWG200, respectively) and the PCW LT-MZI with a sensing arm length of 20 $\mu \rm m$ (designated as PCW20Sim). Experimental values for SWWG LT-MZI with 200- $\mu \rm m$ sensing arm length are designated as SWWG200Expt and for 2-D PCW LT-MZI as PCW20Expt. Simulated values are plotted with solid circles. Experimental values are plotted with open circles.

achieved when wavelength shifts saturate due to no further significant change in overlap between the optical mode and

the analyte. The difference between $\Delta n_{\rm max}$ (in RIU) and LOD (in RIU) determines the measurement range of the systems. In our measured LT-MZI devices, the 2-D PCW LT-MZI can measure a larger $\Delta n_{\rm max}$ than the SWWG LT-MZI.

V. CONCLUSION

In summary, we experimentally validated the performance of foundry-fabricated LT-MZI sensors using slow light 2-D PCW and high fill factored subwavelength waveguide sensing arms. Foundry fabrication with consistent grating coupler performance and better tolerance on fabrication helps to establish that in our sensor devices, the SNR in 20- μ m-long 2-D PCW devices is comparable to 200- μ m-long SWWG devices with both devices exhibiting ~ 10 -dB insertion loss in the loopterminated Mach-Zehnder configuration. Experimentally, 2-D PCW LT-MZI and SWWG LT-MZI demonstrated limits of detection 3.4×10^{-4} and 2.3×10^{-4} RIU, respectively. We showed that by on-chip integration of light sources and photodetectors, both devices can achieve limits of detection 10^{-7} RIU by monitoring intensity changes. It may be noted here that microcavity resonators have also demonstrated 10^{-4} RIU LOD, with LOD $\sim 10^{-7}$ RIU estimated from RR sensors. Achieving such LODs in RR microcavity sensors typically requires extremely high Q-factors exceeding 25 000, which imposes other system requirements on accurate temperature control. Interferometer sensors in comparison have low Q interference fringes that are less susceptible to temperature drifts and are primarily amplitude noise limited. The use of fixed wavelength intensity sensing also eliminates the requirement of wavelength discrimination with high-resolution spectrometers and broadband sources or with high-resolution tunable lasers. Similar RIUs are achieved in slow wave interferometer sensors with practically the same form factors with just a fixed wavelength laser and a photodetector. Fixed wavelength sensing, however, requires the interferometer fringes to be aligned with the source laser wavelength, which can be achieved with zero power consumption using phase change materials for example [39]. Future work will focus on experimental demonstration of the novel loop-terminated Mach–Zehnder and other interferometer architectures, probing the limits of detection in biosensing with fixed wavelength intensity sensing to enable portable and disposable silicon photonic biosensor packages.

ACKNOWLEDGMENT

Jianhao Shen and Asela Perera performed the 2-D photonic crystal waveguide (PCW) and subwavelength waveguide (SWWG) measurements, respectively. Arushi Rai prepared the biosensing samples. Swapnajit Chakravarty conceived the slow wave PCW and subwavelength LT-MZI sensor device concepts. All authors contributed to the writing of the manuscript. The authors would like to thank AIM Photonics for fabricating the passive silicon photonic devices and use of process development kit (PDK) grating couplers.

REFERENCES

[1] M. Iqbal et al., "Label-free biosensor arrays based on silicon ring resonators and high-speed optical scanning instrumentation," *IEEE J. Sel. Topics Quantum Electron.*, vol. 16, no. 3, pp. 654–661, May 2010, doi: 10.1109/JSTQE.2009.2032510.

- [2] R. Guider et al., "Sensitivity and limit of detection of biosensors based on ring resonators," Sens. Bio-Sens. Res., vol. 6, pp. 99–102, Dec. 2015, doi: 10.1016/J.SBSR.2015.08.002.
- [3] S. Chakravarty, J. Topol'ancik, P. Bhattacharya, S. Chakrabarti, Y. Kang, and M. E. Meyerhoff, "Ion detection with photonic crystal microcavities," *Opt. Lett.*, vol. 30, no. 19, p. 2578, Oct. 2005, doi: 10.1364/OL.30.002578.
- [4] M. R. Lee and P. M. Fauchet, "Two-dimensional silicon photonic crystal based biosensing platform for protein detection," *Opt. Exp.*, vol. 15, no. 8, p. 4530, 2007, doi: 10.1364/OE.15.004530.
- [5] S. Chakravarty et al., "Multiplexed specific label-free detection of NCI-H358 lung cancer cell line lysates with silicon based photonic crystal microcavity biosensors," *Biosensors Bioelectron.*, vol. 43, pp. 50–55, May 2013, doi: 10.1016/J.BIOS.2012.11.012.
- [6] L. Huang et al., "Improving the detection limit for on-chip photonic sensors based on subwavelength grating racetrack resonators," *Opt. Exp.*, vol. 25, no. 9, p. 10527, May 2017, doi: 10.1364/OE.25.010527.
- [7] J. Flueckiger et al., "Sub-wavelength grating for enhanced ring resonator biosensor," Opt. Exp., vol. 24, no. 14, p. 15672, Jul. 2016, doi: 10.1364/OE.24.015672.
- [8] J. Homola, S. S. Yee, and G. Gauglitz, "Surface plasmon resonance sensors: Review," *Sens. Actuators B, Chem.*, vol. 54, p. 3, 1999.
- [9] K. Zinoviev, L. G. Carrascosa, J. Sánchez del Río, B. Sepulveda, C. Domínguez, and L. M. Lechuga, "Silicon photonic biosensors for labon-a-chip applications," *Adv. Opt. Technol.*, vol. 2008, no. 1, pp. 1–6, Jan. 2008, doi: 10.1155/2008/383927.
- [10] M. J. Goodwin, G. A. J. Besselink, F. Falke, A. S. Everhardt, J. J. L. M. Cornelissen, and J. Huskens, "Highly sensitive protein detection by asymmetric Mach–Zehnder interferometry for biosensing applications," ACS Appl. Bio Mater., vol. 3, no. 7, pp. 4566–4572, Jul. 2020, doi: 10.1021/ACSABM.0C00491.
- [11] K. Schmitt, B. Schirmer, C. Hoffmann, A. Brandenburg, and P. Meyrueis, "Interferometric biosensor based on planar optical waveguide sensor chips for label-free detection of surface bound bioreactions," *Biosensors Bioelectron.*, vol. 22, no. 11, pp. 2591–2597, May 2007, doi: 10.1016/j.bios.2006.10.016.
- [12] A. Densmore et al., "Silicon photonic wire biosensor array for multiplexed real-time and label-free molecular detection," *Opt. Lett.*, vol. 34, no. 23, p. 3598, Dec. 2009, doi: 10.1364/ol. 34.003598.
- [13] K. Qin, S. Hu, S. T. Retterer, I. I. Kravchenko, and S. M. Weiss, "Slow light Mach–Zehnder interferometer as label-free biosensor with scalable sensitivity," *Opt. Lett.*, vol. 41, no. 4, p. 753, Feb. 15, 2016, doi: 10.1364/ol.41.000753.
- [14] L. Torrijos-Morán, A. Griol, and J. García-Rupérez, "Slow light bimodal interferometry in one-dimensional photonic crystal waveguides," *Light*, *Sci. Appl.*, vol. 10, no. 1, p. 16, Jan. 2021, doi: 10.1038/s41377-020-00460-y
- [15] M. Kitsara, K. Misiakos, I. Raptis, and E. Makarona, "Integrated optical frequency-resolved Mach-Zehnder interferometers for label-free affinity sensing," *Opt. Exp.*, vol. 18, no. 8, p. 8193, Apr. 2010, doi: 10.1364/oe.18.008193.
- [16] J. Shen, D. Donnelly, and S. Chakravarty, "Slow-wave-enhanced on-chip Michelson interferometer sensor," *Opt. Lett.*, vol. 48, no. 22, p. 5968, Nov. 2023, doi: 10.1364/ol.500033.
- [17] W.-C. Lai, S. Chakravarty, X. Wang, C. Lin, and R. T. Chen, "Photonic crystal slot waveguide absorption spectrometer for on-chip near-infrared spectroscopy of Xylene in water," *Appl. Phys. Lett.*, vol. 98, no. 2, Jan. 2011, Art. no. 023304, doi: 10.1063/1.3531560.
- [18] O. S. Magaña-Loaiza et al., "Enhanced spectral sensitivity of a chip-scale photonic-crystal slow-light interferometer," *Opt. Lett.*, vol. 41, no. 7, p. 1431, Apr. 2016, doi: 10.1364/ol.41.001431.
- [19] M. Florjanczyk, P. Cheben, S. Janz, A. Scott, B. Solheim, and D.-X. Xu, "Multiaperture planar waveguide spectrometer formed by arrayed Mach–Zehnder interferometers," *Opt. Exp.*, vol. 15, no. 26, p. 18176, Dec. 24, 2007, doi: 10.1364/OE.15.018176.
- [20] Y. Zou, S. Chakravarty, L. Zhu, and R. T. Chen, "The role of group index engineering in series-connected photonic crystal microcavities for high density sensor microarrays," *Appl. Phys. Lett.*, vol. 104, no. 14, Apr. 2014, Art. no. 141103, doi: 10.1063/ 1.4871012.
- [21] S. Chakravarty, Y. Zou, W.-C. Lai, and R. T. Chen, "Slow light engineering for high Q high sensitivity photonic crystal microcavity biosensors in silicon," *Biosensors Bioelectron.*, vol. 38, no. 1, pp. 170–176, Oct. 2012, doi: 10.1016/J.BIOS.2012.05.016.

- [22] Z. Zhang, Y. Wang, and H. K. Tsang, "Ultracompact 40-channel arrayed waveguide grating on silicon nitride platform at 860 nm," *IEEE J. Quantum Electron.*, vol. 56, no. 1, pp. 1–8, Feb. 2020, doi: 10.1109/JQE.2019.2951034.
- [23] J. Shen et al., "Phase-change-material integrated, phase-error corrected, resolution-enhanced Michelson interferometer Fourier transform spectrometer," in *Proc. Conf. Lasers Electro-Optics Society*, 2024, pp. 1–24.
- [24] Y. Ma, B. Dong, and C. Lee, "Progress of infrared guided-wave nanophotonic sensors and devices," *Nano Converg.*, vol. 7, no. 1, p. 12, Apr. 2020, doi: 10.1186/S40580-020-00222-X.
- [25] F. Vollmer and S. Arnold, "Whispering-gallery-mode biosensing: Label-free detection down to single molecules," *Nature Methods*, vol. 5, no. 7, pp. 591–596, Jul. 2008, doi: 10.1038/NMETH.1221.
- [26] X. Fan, I. M. White, S. I. Shopova, H. Zhu, J. D. Suter, and Y. Sun, "Sensitive optical biosensors for unlabeled targets: A review," *Analytica Chim. Acta*, vol. 620, nos. 1–2, pp. 8–26, Jul. 2008, doi: 10.1016/J.ACA.2008.05.022.
- [27] C. Caucheteur, T. Guo, and J. Albert, "Review of plasmonic fiber optic biochemical sensors: Improving the limit of detection," *Anal. Bioanal. Chem.*, vol. 407, no. 14, pp. 3883–3897, May 2015, doi: 10.1007/S00216-014-8411-6.
- [28] D. Gallegos et al., "Label-free biodetection using a smartphone," *Lab Chip*, vol. 13, no. 11, p. 2124, 2013, doi: 10.1039/C3LC40991K.
- [29] S. Chakravarty, A. Hosseini, X. Xu, L. Zhu, Y. Zou, and R. T. Chen, "Analysis of ultra-high sensitivity configuration in chip-integrated photonic crystal microcavity bio-sensors," *Appl. Phys. Lett.*, vol. 104, no. 19, May 2014, Art. no. 191109, doi: 10.1063/1.4875903.
- [30] D. Huang et al., "High-power sub-kHz linewidth lasers fully integrated on silicon," *Optica*, vol. 6, no. 6, p. 745, 2019, doi: 10.1364/OPTICA.6.000745.
- [31] C. Xiang et al., "3D integration enables ultralow-noise isolator-free lasers in silicon photonics," *Nature*, vol. 620, no. 7972, pp. 78–85, Aug. 2023, doi: 10.1038/S41586-023-06251-W.
- [32] R. Tian et al., "Chip-integrated van der Waals PN heterojunction photodetector with low dark current and high responsivity," *Light, Sci. Appl.*, vol. 11, no. 1, p. 101, Apr. 2022, doi: 10.1038/S41377-022-00784-X.
- [33] K. Sun et al., "Low dark current III–V on silicon photodiodes by heteroepitaxy," *Opt. Exp.*, vol. 26, no. 10, p. 13605, May 2018, doi: 10.1364/oe.26.013605.
- [34] M. Y. Plotnikov and A. V. Volkov, "Adaptive phase noise cancellation technique for fiber-optic interferometric sensors," *J. Lightw. Technol.*, vol. 39, no. 14, pp. 4853–4860, Jul. 15, 2021, doi: 10.1109/JLT.2021.3075781.
- [35] J. Leuermann et al., "Optimizing the limit of detection of waveguide-based interferometric biosensor devices," *Sensors*, vol. 19, no. 17, p. 3671, Aug. 2019, doi: 10.3390/S19173671.
- [36] I. Molina-Fernández, J. Leuermann, A. Ortega-Moñux, J. G. Wanguemert-Pérez, and R. Halir, "Fundamental limit of detection of photonic biosensors with coherent phase read-out," *Opt. Exp.*, vol. 27, no. 9, p. 12616, 2019, doi: 10.1364/OE.27.012616.
- [37] M. Scullion, T. Krauss, and A. Di Falco, "Slotted photonic crystal sensors," *Sensors*, vol. 13, no. 3, pp. 3675–3710, Mar. 2013, doi: 10.3390/S130303675.
- [38] T. Claes, W. Bogaerts, and P. Bienstman, "Experimental characterization of a silicon photonic biosensor consisting of two cascaded ring resonators based on the Vernier-effect and introduction of a curve fitting method for an improved detection limit," *Opt. Exp.*, vol. 18, no. 22, p. 22747, Oct. 2010, doi: 10.1364/OE.18.022747.
- [39] J. Shen et al., "Phase-change-material trimmed, fixed-wavelength slow wave Michelson interferometer sensors for low-cost chem-bio sensing applications," in *Proc. Conf. Lasers Electro-Opt. Soc.*, 2024, pp. 1–23.

Jianhao Shen (Student Member, IEEE) received the B.S. degree in electro-optics from the Huazhong University of Science and Technology (HUST), Wuhan, China, in 2020, and the M.S. degree in electro-optics and photonics from the University of Dayton, Dayton, OH, USA, in 2022, where he is pursuing the Ph.D. degree with the Department of Electro-Optics and Photonics.

His research interests include integrated photonics device design, manufacturing, and measurements.

Asela Perera received the B.S. degree in computational physics from the University of Colombo, Colombo, Sri Lanka, in 2019, and the M.S. degree in electrical and computer engineering from Sungkyunkwan University, Suwon, South Korea, in 2021. He is currently pursuing the Ph.D. degree with the Department of Electro-Optics and Photonics, University of Dayton, Dayton, OH, USA.

His research interests are in silicon photonic devices for chem-bio sensing and computing applications.

Arushi Rai received the B.E. degree in biotechnology from Amity University, Noida, India, in 2016, and the M.E. degree in biotechnology from BITS Pilani, Pilani, India, in 2019. She is pursuing the Ph.D. degree with the Department of Biology, University of Dayton, Dayton, OH, USA, working under the guidance of Dr. Madhuri Kango-Singh.

Before doctoral studies, she gained experience as a Scientist-2 at Strand Life Sciences, Bengaluru, Karnataka, India, where her work involved interpretation, analysis, and curation of scientific literature related to genomic variants and cancer research. She has made contributions to the field of biological research, including co-authoring several book chapters, reviews, and research articles. She has presented her research at numerous national and international conferences, showcasing her findings on oncogenic pathways and tumor growth modulation in Drosophila cancer models. Her research focuses on the Yorkie-dependent transcriptional network and its role in promoting tumor growth, particularly on epithelial and intestinal tumors using Drosophila as a model organism.

Madhuri Kango-Singh received the Ph.D. degree in molecular genetics from Devi Ahilya University, Indore, India, in 1997.

She did her postdoctoral training at premier international research institutes—the Indian Institute of Sciences, Bengaluru, India; Academia Sinica, Taipei, Taiwan; and The University of Texas MD Anderson Cancer Center, Houston, TX, USA. She is a Professor of Genetics and Cancer Biology at the Department of Biology, University of Dayton, Dayton, OH, USA. She has contributed as an editor for books, an academic editor for research journals, a guest editor for special issues of research journals, and peer-reviewed for multiple journals. She has secured extramural grants from notable institutions including federal agencies such as the National Eye Institute, the National Cancer Institute, and foundations (Knight Templar Eye Foundation); and intramural support from the STEM-Catalyst Grant, Hanley Sustainability Institute, University of Dayton. Her research is focused on the regulation of growth and tissue size during development and in diseases such as cancer and neurodegeneration; and chem-bio sensing for applications in cancer.

Swapnajit Chakravarty (Senior Member, IEEE) received the B.E. degree in electrical engineering from Jadavpur University, Kolkata, India, in 2001, the M.S. degree in electrical engineering (electronic materials and devices) from the University of Cincinnati, Cincinnati, OH, USA, in 2003, and the Ph.D. degree in electrical engineering, specializing in optoelectronics and nanophotonics, from the University of Michigan, Ann Arbor, MI, USA, in 2007.

Prior to joining the University of Dayton, Dayton, OH, USA, in 2021, he held a Principal Research Scientist position at IMEC-USA, Orlando, FL, USA. He is an Associate Professor at the Department of Electro-Optics and Photonics, University of Dayton. He has more than 150 publications in refereed journals and conferences. He holds 12 issued and pending patents on various aspects of nanophotonic sensing. He has been an Active Researcher in integrated nanophotonic devices. His research has covered various nanophotonic lasers, light emitters, chem-bio sensors, on-chip spectrometers on silicon photonics, lithium niobate, and III—V material platforms and hybrids. Currently, he investigates the hybrid integration of advanced materials for applications in computing, communications, and chem-bio sensing/spectroscopy.

Dr. Chakravarty is a Senior Member of SPIE and Optica.